Hydroisomerization of n-Hexadecane Over Nickel-Modified SAPO-11 Molecular Sieve-Supported NiWS Catalysts: Effects of Modification Methods

Xiaojun Dai, Yan Cheng, Meng Si, Qiang Wei* and Yasong Zhou

State Key Laboratory of Heavy Oil Processing, China University of Petroleum, Beijing, China

The complexation-excessive impregnation modification method, which was original in this study, and the ion-exchange method and the *in situ* modification method were used to synthesize Ni-modified SAPO-11 molecular sieves. With the Ni-modified SAPO-11 samples as support, the corresponding NiWS-supported catalysts for the hydroisomerization of n-hexadecane were prepared. The effects of Ni-modification on SAPO-11 characteristics and the active phase were studied. The structure, morphology, and acidity of SAPO-11, as well as the interaction between active metals and support, the morphology, dispersibility, and stacking number of the active phase, were all changed by Ni-modification methods. The complexation-excessive impregnation modification method deleted a portion of Al from SAPO-11 molecular sieves while simultaneously integrating Ni into the skeletal structure of the surface layer of SAPO-11 molecular sieves, considerably enhancing the acidity of SAPO-11 molecular sieves. Furthermore, during dealumination, ethylenediaminetetraacetic acid generated more mesoporous structures and increased the mesoporous volume of SAPO-11 molecular sieves. Because the complexation-excessive impregnation modification method increased the amount of Ni in the surface framework of the SAPO-11 molecular sieve, it has weakened the interaction between the active phase and the support, improved the properties of the active phase, and greatly improved the hydroisomerization performance of NiW/NiSAPO-11. The yield of i-hexadecane of NiW/NiSAPO-11 increased by 39.3% when compared to NiW/NiSAPO-11. It presented a realistic approach for increasing the acidity of SAPO-11, reducing the interaction between active metals and support, and improving the active phase stacking problem.

Keywords: Ni-modified, SAPO-11, NiWS-supported catalyst, active phase, hydroisomerization

INTRODUCTION

The presence of long-chain n-alkanes is thought to be the cause of the high freezing point of diesel and the poor low-temperature fluidity of lubricating base oil (Tao et al., 2017). The formation of branched isomers by hydroisomerization of long-chain n-alkanes can effectively lower the freezing point of diesel and increase the low-temperature fluidity of lubricating base oil (Du et al., 2018). The

bifunctional catalyst for the hydroisomerization of n-alkanes contains an acid site for the skeletal isomerization of olefin intermediates and a metal site for de/hydrogenation (Wei et al., 2017). Acidic supports, such as zeolites, usually supply acid sites, whereas noble metals or other transition metals give metal sites (Yang et al., 2017a). Because of their one-dimensional porosity and low acidity, SAPO-11 molecular sieves are commonly employed as a support for n-alkane hydroisomerization catalysts (Guo et al., 2012). Noble metals like platinum and palladium have strong de/hydrogenation activities, whereas nonnoble metals like nickel are also used as metal components in hydroisomerization catalysts (Zhao et al., 2014; Wang et al., 2018).

Although SAPO-11 molecular sieves have been used in industry and have shown to be a solid support for hydroisomerization catalysts, increasing their performance in hydroisomerization is still a concern worth investigating (Blasco et al., 2006). The active sites for catalyzing isomerization of the alkane molecular skeleton are thought to be Brnsted (B) acid sites in the SAPO-11 molecular sieve, particularly the medium strength B acid sites (Guo et al., 2013). As a result, improving the isomerization performance of SAPO-11 requires a better understanding of enhancing the proportion of medium and strong B acid sites. Lyu et al. (2019a) used *in situ* synthesis to introduce varying amounts of Ni into SAPO-11 to investigate the effects of metal-acid balance on n-hexane hydroisomerization and the acidity of SAPO-11. However, up to now, no one has studied the effects of modification methods in the process of Ni modification on the physicochemical properties (such as textural and acidity) of SAPO-11 molecular sieves. Furthermore, despite the remarkable catalytic activity of noble metals as metal components of hydroisomerization catalysts, there are two issues. On the one hand, the high cost of noble metals restricts their use in industry (Tian and Chen., 2014). Noble metals, on the other hand, are poisoned and inactivated due to their sensitivity to sulfur-containing compounds in raw materials (Yang et al., 2017b; Lyu et al., 2020). Although some researchers have reported employing Ni as a metal component instead of noble metals, hydroisomerization results revealed that Ni has a high hydrogenolysis activity, resulting in lower isomer selectivity and yield than noble metal-supported catalysts (Karthikeyan et al., 2016; Yang et al., 2017c). Transition metal sulfides have a good de/hydroisomerization performance and are widely used as the active phase of catalysts for hydrodesulfurization (Díaz de León et al., 2017), hydrodenitrogenation, and hydrocracking (Cui et al., 2019), such as NiMoS (Zhou et al., 2017) and NiWS (Minaev et al., 2019). In the past, there have been many reports on the application of noble metal (Pt, Pd) or Ni-supported catalysts in alkane hydroisomerization (Lyu et al., 2017; Hongloi et al., 2021), but there have been few on the application of transition metal sulfide catalysts in alkane hydroisomerization and the effects of the properties of the transition metal sulfide active phase on alkane hydroisomerization (Shi et al., 2009; Tan et al., 2021).

In this study, the ion-exchange method, the *in situ* modification method, and the complexation-excessive impregnation modification method were used to modify SAPO-11 molecular sieves with Ni in this study. The hydroisomerization of n-hexadecane was carried out using the Ni-modified SAPO-11 molecular sieves, which were supported by NiWS. The impact of various modification methods on the physicochemical properties of SAPO-11, the active phase properties, and the hydroisomerization performance of several catalysts were studied.

EXPERIMENTAL

Materials

Phosphoric acid (H_3PO_4, 85wt%; Aladdin), pseudo-boehmite (Al_2O_3, 70wt%; Macklin), acid silica sol (SiO_2, 30wt%; Dezhou Jinghuo technology Glass Co., Ltd.), di-n-propylamine (DPA, 99wt%; Aladdin), diisopropylamine (DIPA, 99wt%; Aladdin), dodecyltrimethylammonium bromide (DTAB, 99wt%; Aladdin), ammonium chloride (NH_4Cl, 99.5wt%; Macklin), nickel nitrate hexahydrate($Ni(NO_3)_2 \cdot 6H_2O$, 98wt%; Aladdin), ammonium metatungstate hydrate ($(NH_4)_6H_2W_{12}O_{40} \cdot xH_2O$, 99.5wt%; Macklin), ethylenediaminetetraacetic acid (EDTA, 98wt%; Aladdin), and deionized water.

Synthesis and Modification of SAPO-11 Molecular Sieves

Deionized water and phosphoric acid were mixed in a normal synthesis procedure, then pseudo-boehmite was added to the solution and agitated for 2 h. DPA and DIPA were added and mixed continuously for 2 h. Drop by drop, acid silica sol was added to the system and aggressively agitated for 2 h. Finally, DTAB was added and agitated for 1 h, resulting in an initial gel with the following molar composition: 1.0 Al_2O_3: 0.75 P_2O_5: 0.45 SiO_2: 0.5 DPA: 0.5 DIPA: 0.05 DTAB: 45 H_2O. The gel was pre-crystallized at 90°C for 12 h before being crystallized at 190°C for 24 h. The SAPO-11 molecular sieves were obtained by washing the solid products collected by filtration to neutrality with deionized water, drying them at 110°C overnight, and calcining them at 600°C for 6 h.

For the ion-exchange procedure, 10.0 g of SAPO-11 was mixed with 100 g of 0.3 mol/L nickel nitrate solution, which was then exchanged at 90°C for 4 h, filtered, dried at 110°C overnight, and calcined at 500°C for 4 h. Ni@SAPO-11 was the name given to the dried and calcined sample. The operation procedures for the *in situ* modification method were similar to the above-mentioned SAPO-11 synthesis steps, with the exception that 3% nickel was added during the initial gel formation process (the molar ratio of Ni/Al_2O_3 was 3%). The products were filtered before being dried at 110°C overnight and calcined for 4 h at 500°C. Ni-SAPO-11 was the name given to the dried and calcined sample. 0.1 mol EDTA was added to 50 ml of 0.3 mol/L nickel nitrate solution for the complexation-excessive impregnation modification procedure, and then 10 g of SAPO-11 molecular sieve particles with 20–40 mesh were impregnated with the resulting solution. SAPO-11 molecular sieve particles after complexation-excessive

impregnation were obtained by filtration, dried, and calcined, and designated NiSAPO-11 after soaking for 4 h.

Preparation of NiW-Supported Catalysts

The SAPO-11, Ni@SAPO-11, and Ni-SAPO-11 particles were pressed, crushed, and sieved to a size of 20–40 mesh. The NiW-supported catalysts were made using the incipient-wetness impregnation method with an aqueous solution of nickel nitrate hexahydrate and ammonium metatungstate hydrate, then dried at 110°C for 6 h and calcined at 500°C for 4 h after being evaporated at room temperature overnight. The loading concentration of NiO was 5% and the loading concentration of WO_3 was 15% for each catalyst. NiW/SAPO-11, NiW/Ni@SAPO-11, NiW/Ni-SAPO-11, and NiW/NiSAPO-11 were the names given to the resulting catalysts.

Characterization

The SAPO-11 samples were characterized by X-ray diffraction (XRD) on a Bruker AXS D8 Advance X-ray diffractometer using Cu Kα radiation at 40 kV and 40 mA, and 2θ varied from 5 to 90° at a scanning speed of 5°/min. On a field-emission environmental scanning electron microscope, images of the SAPO-11 samples were taken using scanning electron microscopy (SEM) (FEI Quanta 200F). After degassing the materials at 350°C under vacuum for 15 h, N_2 adsorption-desorption measurements were performed on a Micromeritics ASAP 2020 analyzer at −196°C. The Brunauer-Emmett-Teller (BET) and de Boer t-plot methods were used to compute the specific surface area and micropore volume, respectively, while the Barrett-Joyner-Halenda technique was used to calculate the mesopore volume. A Micromeritics auto-chem 2920 device was used to analyze temperature-programmed desorption of ammonia (NH_3-TPD). The sample was heated to 600°C in an Ar flow for 30 min, then switched to an ammonia flow for another 30 min before being cooled to 70°C. The sample was purged with Ar for 2 h to eliminate the physically adsorbed ammonia, and the TPD signal was recorded using a thermal conductivity detector with a heating rate of 10°C/min from 70 to 600°C. A Nicolet 5700 spectrometer was used to record Pyridine adsorbed infrared (Py-IR) spectra. At 200 and 350°C, the pyridine samples were evacuated. On a Quantachrome Autosorb-iQ-C chemical adsorption system, temperature-programmed hydrogen reduction (H_2-TPR) measurements were taken. The samples were heated at a rate of 10°C/min in an H_2-Ar flow containing 5% H_2 from room temperature to 1,050°C. The presulfurized catalysts were analyzed using X-ray photoelectron spectroscopy (XPS) on a Thermo spectrometer using Al Kα radiation as the excitation light source. To calibrate the binding energy scale, all spectra used the Al 2p peak with a binding energy of 74.6 eV. The presulfurized catalysts' XPS spectra were decomposed using XPS PEAK, and the deconvolution was achieved using Gaussian-Lorentzian band shapes. A JEM 2100 LaB$_6$ transmission electron microscope was used to obtain high-resolution transmission electron microscope (HRTEM) images of the presulfurized catalysts. The average length and average stacking number of WS$_2$ slabs were determined using methods described in the literature (Yu et al., 2012):

$$\text{Average slab length } \bar{L} = \frac{\sum_{i=1}^{n} n_i l_i}{\sum_{i=1}^{n} n_i} \qquad (1)$$

$$\text{Average stacking number } \bar{N} = \frac{\sum_{i=1}^{n} n_i N_i}{\sum_{i=1}^{n} n_i} \qquad (2)$$

where l_i denotes the WS$_2$ slab length, n_i denotes the number of slabs of length l_i, and N_i is the number of layers in a WS$_2$ slab. The dispersion degree of the WS$_2$ active phase, f_W, was derived using the following equation, assuming that the WS$_2$ slabs are presented as perfect hexagons (Tao et al., 2014):

$$f_W = \frac{W_{edge}}{W_{total}} = \frac{\sum_{i=1}^{t} 6(n_i - 1)}{\sum_{i=1}^{t} (3n_i^2 - 3n_i + 1)} \qquad (3)$$

where W_{edge} denotes the W atoms on the edges of WS$_2$ slabs, W_{total} denotes the total number of W atoms, n_i denotes the number of W atoms along one side of a WS$_2$ slab determined by its length [L = 3.2 (2ni—1) Å], and t denotes the total number of slabs determined by at least 500 WS$_2$ slabs obtained from HRTEM images of various catalysts.

Catalytic Performance Assessment

In a fixed-bed hydrogenation micro-reactor, the hydroisomerization of n-hexadecane (n-C_{16}) was carried out. In a typical reaction, the tubular furnace held 9.0 ml of catalyst and 22 ml of silica sand. The catalyst was presulfurized using a CS_2 cyclohexane solution containing 2% CS_2 at 320°C and 4 MPa for 5 h with a liquid hourly space velocity (LHSV) of 7 h^{-1} and an H_2/oil ratio of 100 (v/v) before the reaction. After presulfurization, the catalytic performance of the catalyst was examined at 2 MPa, 1.5 h^{-1} LHSV, 600 (v/v) H_2/oil, and 320–400°C reaction temperature. When the temperature was reduced to the reaction temperature, a syringe pump was used to feed the reactant n-hexadecane into the reactor. The products were analyzed using a Shimadzu GC-2014 gas chromatograph with a capillary HP-PONA column and GC-MS for qualitative analysis. The TOF (turnover frequency, which is used to evaluate the catalytic activity of a catalyst) of each active site was calculated using the following equation based on the number of all available active sites and the conversion of n-C_{16} of each catalyst at 340°C (Wen et al., 2020):

$$TOF = \frac{V_{feed} \cdot x}{n_W \cdot f_W} \qquad (4)$$

where V_{feed} is the feed rate of the reactant n-C_{16} in mol/h, x is the conversion of n-C_{16} at 340°C, n_w is the amount of W atom in the catalyst in mol, and f_W is the dispersion degree of W species. The following equation was used to compute the hydroisomerization reaction rate constant (Pimerzin et al., 2019):
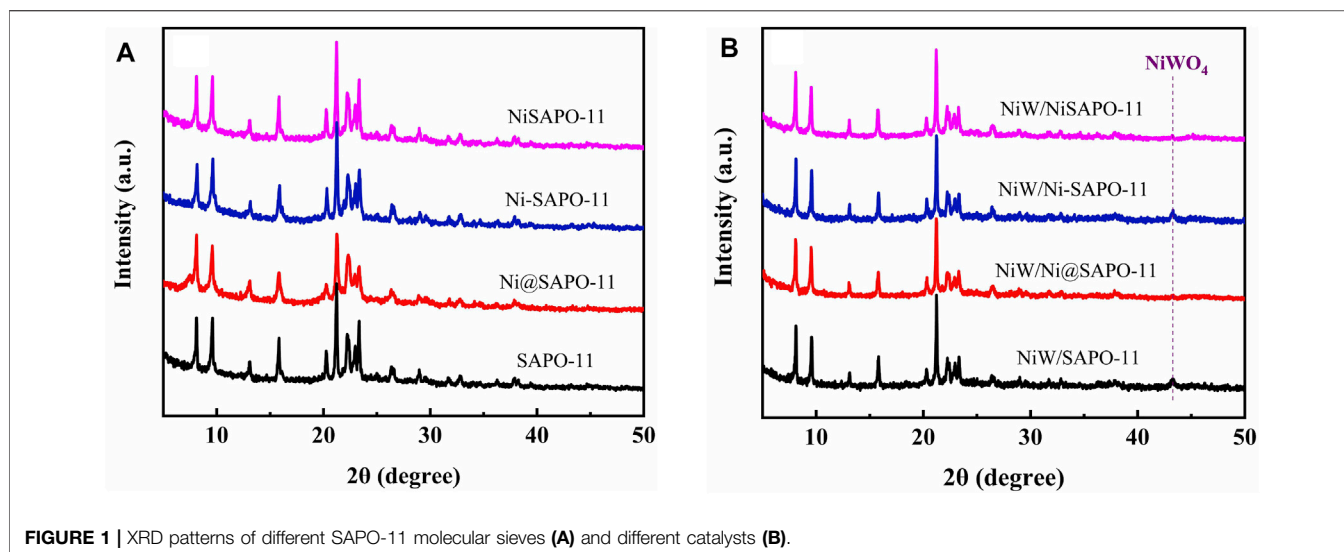
FIGURE 1 | XRD patterns of different SAPO-11 molecular sieves **(A)** and different catalysts **(B)**.

$$k_{iso} = \frac{V_{feed}}{m} \ln(1-x) \qquad (5)$$

where k_{iso}, V_{feed}, m and x are the quasi-first-order reaction rate constant of n-C_{16} hydroisomerization on different catalysts, the feed flow rate of the reactant n-C_{16} in mol/h, the mass of catalyst and the conversion of n-C_{16}, respectively.

RESULTS AND DISCUSSION

Phase Structure

The XRD patterns of Ni-modified SAPO-11 molecular sieves generated by various ways are shown in **Figure 1A**. All samples exhibited diffraction peaks in the 2θ range of 5–50° that were assigned to the normal AEL structure, demonstrating that SAPO-11 samples retained full structural units after Ni alteration by various methods (Lyu et al., 2019b). The prominent characteristic diffraction peaks of Ni-SAPO-11 indicate that it has a high crystallinity (Song et al., 2017). Because Ni species replaced a portion of Al species in the SAPO-11 framework, crystalline Ni species resulted. The strength of the distinctive diffraction peaks of Ni@SAPO-11 reduced slightly when compared to SAPO-11, which could be attributable to a decrease in crystallinity during the ammonium-exchange and nickel ion-exchange processes (rehydration) (Yang et al., 2017c). Furthermore, the intensity of the characteristic diffraction peaks of NiSAPO-11 did not significantly decrease, indicating that EDTA could remove some Al species but not the crystal structure of SAPO-11. A weak characteristic diffraction peak attributed to NiO appeared at 2θ = 37.2° of XRD patterns of all the samples, which indicates that there were a small number of NiO species in all the samples, and the distribution of NiO species in SAPO-11 molecular sieves was relatively uniform. **Figure 1B** shows the XRD spectra of the different catalysts. It can be seen that the different catalysts still retained the characteristic diffraction peaks attributed to AEL structure, indicating that the loading of metal components did

not cause the crystal structure of SAPO-11 molecular sieves to be destroyed. In addition, all the catalysts showed a weak characteristic diffraction peak attributed to NiWO₄ species around 2θ = 43.2°, which indicates that NiWO₄ species existed in all samples and dispersed relatively evenly.

Morphology

SEM images of Ni-modified SAPO-11 molecular sieves generated by various procedures are shown in **Figure 2**. SAPO-11 had pseudospherical particles with a particle size of roughly 5 μm and a fairly uniform particle size distribution. The particle shape of Ni@SAPO-11 was not as regular as that of SAPO-11, and the discrepancy could be due to its particle form being destroyed when it was exchanged in aqueous solution twice. While Ni-SAPO-11 was basically the same as SAPO-11 in particle shape and size. As for NiSAPO-11, a small number of small particles similar to amorphous substances appear in its SEM image, which may be the smaller particles formed by the decomposition of SAPO-11 molecular sieve particles in the process of removing Al species by EDTA.

Textural Properties

Figure 3 shows the N₂ adsorption-desorption isotherms (**Figure 3A**) and pore size distribution (**Figure 3B**) of the Ni-modified SAPO-11 molecular sieves. Isotherms with typical H4-type hysteresis loops were seen in all samples (Chen et al., 2017). At low relative pressure ($10^{-5} \leq P/P_0 \leq 10^{-2}$), the amount of N₂ adsorption in all samples rose dramatically, which was attributable to N₂ filling the micropores (Du et al., 2019). Within the relative pressure P/P_0 range of 0.4–0.9, all samples showed clear hysteresis loops, showing that these samples have a lot of mesopores (Wen et al., 2019). The hysteresis loop of NiSAPO-11 is clearly larger than that of other samples, indicating that NiSAPO-11 has a more mesoporous structure than other samples. This is because, when eliminating Al species, EDTA dissolved and etched in the crystals of SAPO-11 molecular sieves, forming many new mesoporous structures. **Figure 3B**
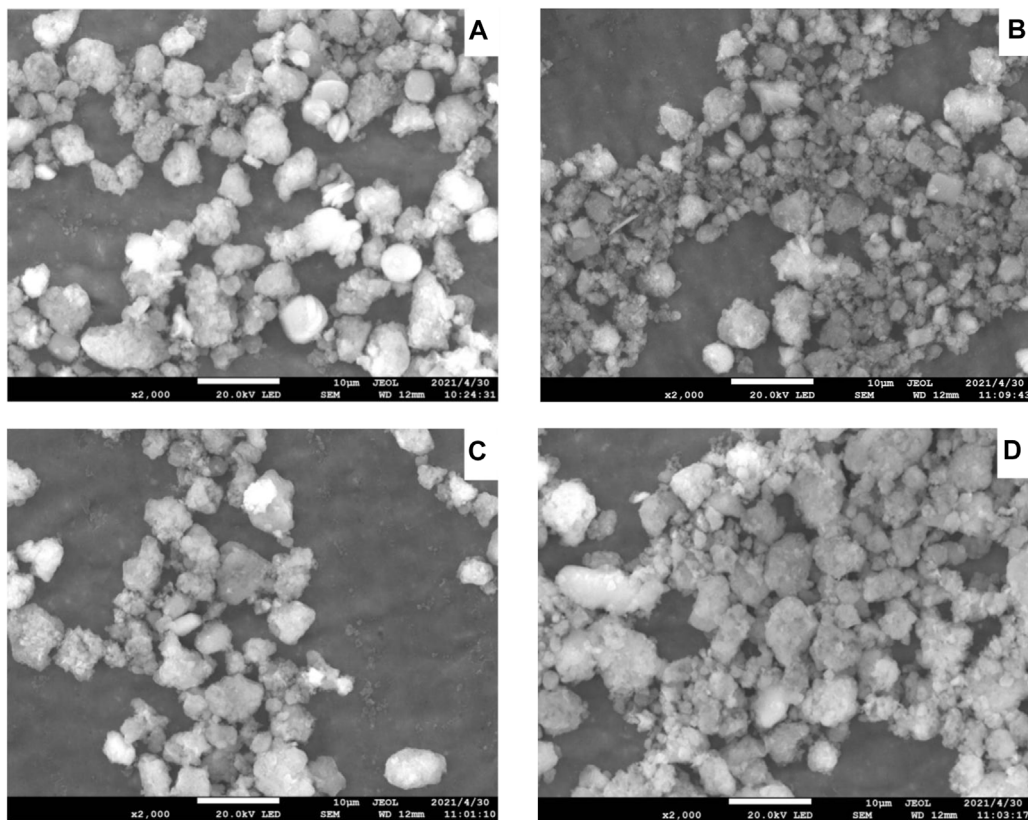
FIGURE 2 | SEM images of Ni-modified SAPO-11: **(A)** SAPO-11, **(B)** Ni@SAPO-11, **(C)** Ni-SAPO-11, and **(D)** NiSAPO-11.
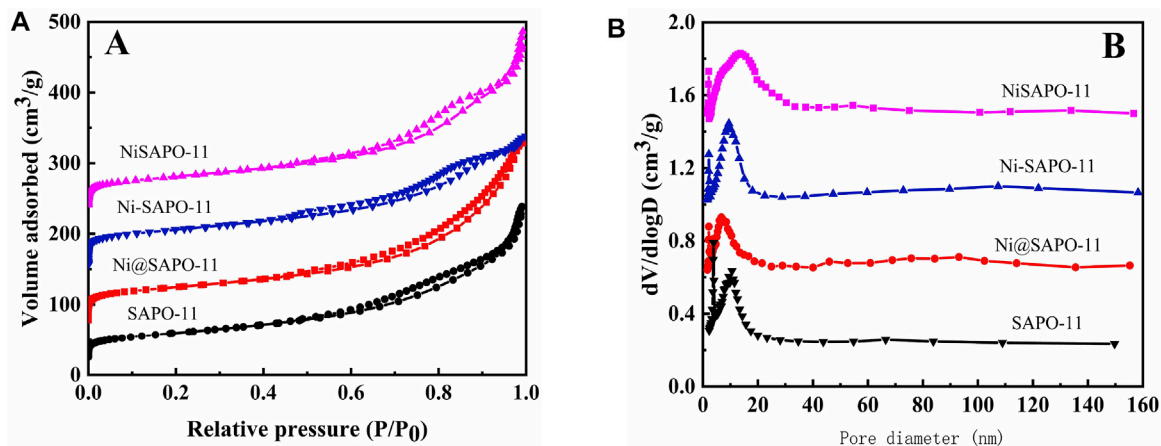
FIGURE 3 | N_2 adsorption-desorption isotherms **(A)** and pore size distribution **(B)** of Ni-modified SAPO-11 molecular sieves.
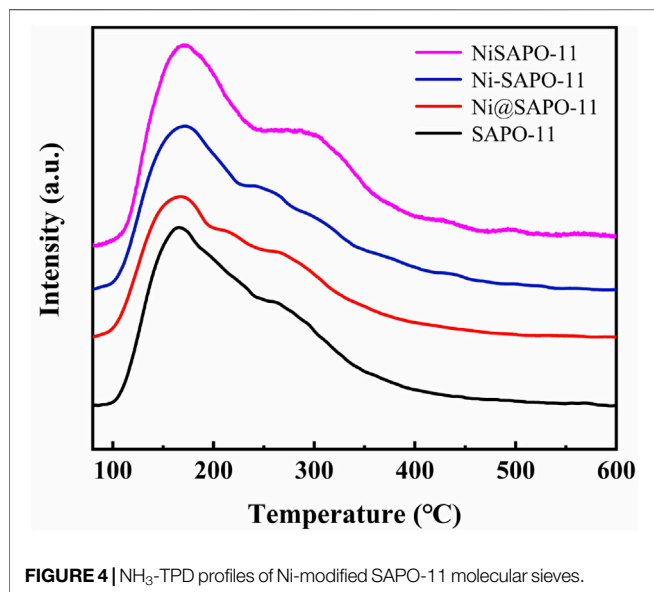
shows the pore size distribution of all samples, with the pore size of SAPO-11, Ni@SAPO-11, and Ni-SAPO-11 primarily dispersed around 12 nm. The foregoing findings show that these samples include hierarchical micro-mesoporous structures. However, the mesoporous size of NiSAPO-11 is centered at 18 nm, which is larger than that of other samples, implying that EDTA does have a pore-expansion role.

The BET surface area (S_{BET}), exterior surface area (S_{ext}), and pore volume of the Ni-modified SAPO-11 are shown in **Table 1**. The S_{BET} and pore volume of Ni@SAPO-11 were reduced to some

TABLE 1 | Textural properties of Ni-modified SAPO-11.

Sample	S_{BET}, m²/g	S_{ext}, m²/g	V_{micro}, cm³/g	V_{meso}, cm³/g	V_{total}, cm³/g
NiSAPO-11	188	96	0.11	0.36	0.47
Ni-SAPO-11	174	94	0.08	0.30	0.38
Ni@SAPO-11	158	88	0.07	0.20	0.27
SAPO-11	166	91	0.09	0.26	0.35

**FIGURE 4 |** NH₃-TPD profiles of Ni-modified SAPO-11 molecular sieves.

extent when compared to SAPO-11. One probable explanation is that Ni species enter the pores, blocking certain micropores and occupying a portion of the mesopore volume (V_{meso}) in the ion-exchange process. Another possibility is that during the ion-exchange process, a portion of the crystal structure collapses, causing the pore channels to fill. The S_{BET} and V_{meso} of Ni-SAPO-11 have increased, indicating that the addition of Ni *in situ* helps to improve the S_{BET} and V_{meso} of SAPO-11 (Liu et al., 2013). The micropore volume (V_{micro}) of Ni-SAPO-11 decreased, implying that some Ni species remain in the micropores and occupy the micropore volume. The S_{BET}, V_{micro}, and V_{meso} of NiSAPO-11 all increased, with V_{meso} increasing by a substantial margin, confirming the prior conclusion that EDTA has the ability to ream and manufacture new mesopores. The S_{BET} and V_{meso} of the different SAPO-11 samples increased in the order of Ni@SAPO-11 < SAPO-11 < Ni-SAPO-11 < NiSAPO-11, indicating that the textural properties of SAPO-11 molecular sieves can be improved most obviously by the complexation-excessive impregnation modification method.

Acidity Properties

The NH₃-TPD measurements were used to determine the acid amounts and acid strength distribution of the Ni-modified SAPO-11 molecular sieves manufactured using various procedures. **Figure 4** shows the NH₃-TPD profiles of the several Ni-modified SAPO-11 samples. Each NH₃-TPD profile revealed two NH₃ desorption peaks about 180 and 310°C,

corresponding to NH₃ adsorbed on weak acid sites, medium and strong acid sites, respectively (Yang et al., 2019). The intensity of the desorption peak represents the acid amount (Li and Wu, 2020). The acid amount of Ni@SAPO-11 was much lower than that of SAPO-11, which was attributable to the fact that part of the acid sites were covered and sheltered by Ni species during Ni ion exchange. The strength of the NH3 desorption peak corresponding to weak acid sites reduced somewhat in Ni-SAPO-11, indicating that the weak acid amount of Ni-SAPO-11 fell slightly (Yang et al., 2017c). This is due to the fact that the acid sites in SAPO-11 are thought to be formed by Si-OH, Al-OH, P-OH, and Si-OH-Al, respectively (Tiuliukova et al., 2018). Some Al precursors were substituted with Ni precursors, resulting in a reduction in acid sites. The intensities of the NH₃ desorption peaks corresponding to medium and strong acid sites increased, indicating that the concentrations of medium and strong acid increased as well. It can be explained by the fact that Ni has a greater average electronegativity (1.91) than Al (1.71), and Ni has a higher covalency than Al. As a result, the Brnsted protons and Lewis caverns generated by Ni substituting part of Al in SAPO-11 have a higher acid density, resulting in more medium and strong acid sites in Ni-SAPO-11. The amount of weak acid, medium and strong acid in NiSAPO-11 were all improved. The increase in weak acid amonut is due to EDTA dredging some blocked channels and establishing new ones, exposing and detecting more acid sites to a large extent. The rise in medium and strong acid amounts in NiSAPO-11 can be attributed to two factors. On the one hand, the exposure of acid sites is caused by an increase in pore volume. In the process of eliminating Al species, EDTA can integrate Ni species into the surface framework of SAPO-11 molecular sieves to generate Ni-OH-Si species, which helps to enhance the density of medium and strong acid in SAPO-11. The results show that the amounts of the weak acid in Ni-modified SAPO-11 decreased in the order of NiSAPO-11 > SAPO-11 > Ni@SAPO-11 > Ni-SAPO-11, while the amounts of medium and strong acid decreased in the order of NiSAPO-11 > Ni-SAPO-11 > SAPO-11 > Ni@SAPO-11.

Py-IR was used to analyze the variations in Brønsted (B) acid sites and Lewis (L) acid sites in the Ni-modified SAPO-11 molecular sieves to determine the acidity of the different SAPO-11 samples (Jin et al., 2018). **Figure 5** shows the Py-IR spectra of the Ni-modified SAPO-11 samples generated using various procedures. Py-IR spectra obtained after pyridine molecules desorbed at 200°C were used to compute the amount of weak acid, whereas Py-IR spectra formed after pyridine molecules desorbed at 350°C were used to calculate the amounts of medium and strong acid. **Table 2** shows the
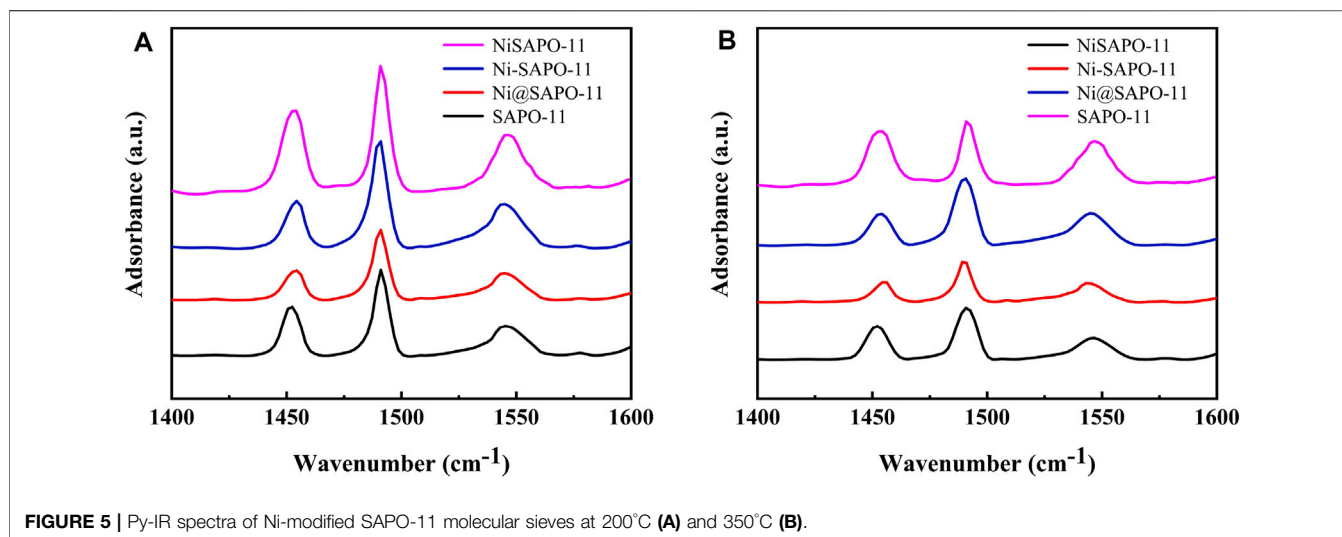
FIGURE 5 | Py-IR spectra of Ni-modified SAPO-11 molecular sieves at 200°C **(A)** and 350°C **(B)**.

TABLE 2 | Acidity properties of Ni-modified SAPO-11 determined by Py-IR.

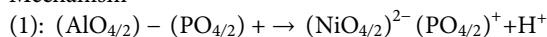| Sample	Acidity (μmol/g)					
	Weak acid sites (200°C)			Medium and strong acid sites (350°C)		
	B	L	B + L	B	L	B + L
SAPO-11	91.87	29.32	121.19	30.62	20.97	51.59
Ni@SAPO-11	53.09	24.25	77.34	23.51	15.11	38.62
Ni-SAPO-11	69.91	35.84	105.75	48.21	18.16	66.37
NiSAPO-11	82.21	56.88	139.09	58.35	24.66	83.01

results of calculating the number of B acid sites and L acid sites and the accompanying findings. All samples had three peaks in the range of 1,400–1,600 cm^{-1}, as illustrated in **Figure 5**. The peaks at 1,455 cm^{-1} and 1,545 cm^{-1} are assigned to pyridine molecules desorbed on L acid sites and B acid sites, respectively (Wen et al., 2020), whereas the peak at 1,490 cm^{-1} is attributed to a combined line of B acid sites and L acid sites (Zhang et al., 2018). The amounts of weak L acid in Ni-modified SAPO-11 molecular sieves decreased in the following order: NiSAPO-11(56.88 μmol/g) > Ni-SAPO-11 (35.84 μmol/g) > SAPO-11 (29.32 μmol/g) > Ni@SAPO-11 (24.25 μmol/g), while the amounts of medium and strong L acid decreased in the following order: NiSAPO-11 (24.66 μmol/g) > SAPO-11 (20.97 μmol/g) > Ni-SAPO-11 (18.16 μmol/g) > Ni@SAPO-11 (15.11 μmol/g). This can be explained by the fact that during the ion-exchange and *in situ* modifications, certain NiO species covered several strong L acid sites. However, some additional weak L acid sites were generated in Ni species in the surface framework of NiSAPO-11, resulting in an increase in the amount of weak L acid and the amount of medium and strong Lacid in NiSAPO-11. The amounts of weak B acid in Ni-modified SAPO-11 molecular sieves decreased in the order of SAPO-11 (91.87 μmol/g) > NiSAPO-11 (82.21 μmol/g) > Ni-SAPO-11 (69.91 μmol/g) > Ni@SAPO-11 (53.09 μmol/g), while the amounts of medium and strong B acid decreased in the order of NiSAPO-11 (58.35 μmol/g) > Ni-SAPO-11 (48.21 μmol/g) > SAPO-11 (30.62 μmol/g) > Ni@SAPO-11

(23.51 μmol/g). In the process of Ni ion exchange (part of H$^+$ being swapped by Ni^{2+}), Ni species covered some weak B acid sites and medium and strong B acid sites, resulting in a decrease in both the amount of weak B acid and the amount of medium and strong B acid (MSB) in Ni@SAPO-11. Some Ni species would undoubtedly cover the acid sites during Ni *in situ* alteration, resulting in a reduction in the number of weak B acid sites in Ni-SAPO-11. Meanwhile, Ni species entered the skeleton structure of SAPO-11 and substituted Al species by mechanism (1) and mechanism (2). Whether it is $(NiO_{4/2})^{2-}(PO_{4/2})^+$ species produced by mechanism (1) substitution or $(HONiO_{4/2})^{2-}(PO_{4/2})^+$ species produced by mechanism (2) substitution, it is beneficial to form more medium and strong B acid sites, which well explains that Ni-SAPO-11 has more medium and strong B acid sites. However, in the process of *in situ* modification, Ni species uniformly enter the bulk and surface framework of SAPO-11 molecular sieves, which is limited to the increase of B acid amount. EDTA only integrates Ni species into the surface framework of SAPO-11 molecular sieves during the complexation-excessive impregnation process, and more Ni species are distributed in the surface framework of SAPO-11 molecular sieves, resulting in a significant improvement of the surface acidity of SAPO-11 molecular sieves, which is the reason why the weak B acid amount, medium and strong B acid amount of NiSAPO-11 reach their maximum. Ni-SAPO-11 modified by Ni by the complexation-excessive impregnation method initiated
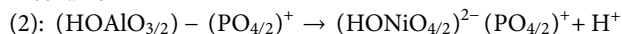
FIGURE 6 | H_2-TPR profiles of the different catalysts.
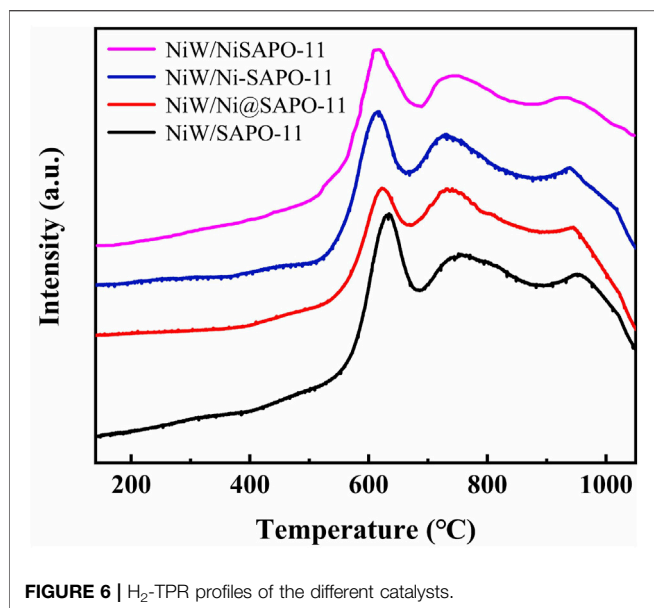
in this study has the largest amount of medium and strong B acid, which is beneficial to improve the catalytic performance of the catalyst.

Mechanism
(1): $(AlO_{4/2}) - (PO_{4/2}) + \rightarrow (NiO_{4/2})^{2-} (PO_{4/2})^{+} + H^{+}$
Mechanism
(2): $(HOAlO_{3/2}) - (PO_{4/2})^{+} \rightarrow (HONiO_{4/2})^{2-} (PO_{4/2})^{+} + H^{+}$

Active Phase Characterization

On bifunctional catalysts, the reducibility of active metals can effectively reflect the interaction between active metals and supports (Yang Z et al., 2019). As a result, H_2-TPR characterization was used to investigate the reducibility of the active metals on the catalysts. **Figure 6** depicts the H_2-TPR profiles of all catalysts. In the range of 0–1,050°C, all samples revealed three hydrogen consumption peaks. The low-temperature reduction peak at 610–635°C is attributed to the reduction of highly dispersed octahedrally coordinated polymeric tungsten species and mostly NiO species, while the moderate-temperature reduction peak at 710–765°C is attributed to the reduction of $NiWO_4$ species, and the high-temperature reduction peak at 930–955°C is attributed to the reduction of refractory tungsten species in the form of W-O-Al (Cui et al., 2013). The results revealed that the low-temperature reduction peaks, moderate-temperature reduction peaks, and high-temperature reduction peaks of the catalysts all migrated to lower temperatures after Ni alteration. The reduction temperatures of low-temperature reduction peaks decreased in the order of NiW/SAPO-11 (634°C) > NiW/Ni@SAPO-11 (624°C) > NiW/Ni-SAPO-11 (611°C) > NiW/NiSAPO-11 (608°C), and the reduction temperatures of moderate-temperature reduction peaks decreased in the order of NiW/SAPO-11 (760°C) > NiW/Ni@SAPO-11 (737°C) > NiW/Ni-SAPO-11 (726°C) > NiW/NiSAPO-11 (723°C), while the reduction temperatures of

high-temperature reduction peaks decreased in the order of NiW/SAPO-11 (957°C) > NiW/Ni@SAPO-11 (944°C) > NiW/Ni-SAPO-11 (936°C) > NiW/NiSAPO-11 (922°C), indicating that the reducibility of active metal NiW on NiW/SAPO-11 catalysts can be improved by introducing Ni into SAPO-11 through the ion-exchange method or the *in situ* modification method.

The sulfided catalysts were studied by HRTEM to visualize the morphologies of the NiWS active phase on the catalysts and compare the dispersibility of sulfided metals on the various Ni-modified SAPO-11 supports. **Figure 7** shows sample HRTEM images of the different supported NiW sulfided catalysts. The WS_2 slab structure is represented by the black line-like layers in the images (Yu et al., 2012). The average length and average stacking number of WS_2 slabs on different catalysts were calculated using statistical analysis (**Eqs 1**, **2**) of at least 500 slabs from different regions of each sulfide catalyst, and the findings are reported in **Table 3**. The results showed that Ni alteration altered the morphologies of the active phase. The average length of WS_2 slabs dropped in the sequence NiW/SAPO-11 (4.62 nm) > NiW/Ni@SAPO-11 (3.95 nm) > NiW/Ni-SAPO-11 (2.98 nm) > NiW/NiSAPO-11 (2.63 nm), whereas the average stacking number rose in the order NiW/SAPO-11 (1.33) < NiW/Ni@SAPO-11 (2.64) < NiW/Ni-SAPO-11 (3.23) < NiW.NiSAPO-11 (3.27). The length of WS_2 slabs on NiW/SAPO-11 ranged from 1 to 7 nm, with the majority falling within the 3–6 nm range. The length of WS_2 slabs on NiW/Ni@SAPO-11 ranged from 1 to 5 nm, with the majority falling between 2 and 5 nm. The length distribution of WS_2 slabs on NiW/Ni-SAPO-11 was 1–4 nm, with the majority in the 2–4 nm region. The length of WS_2 slbs of NiW/NiSAPO-11 ranges between 1–4 nm, but is mainly in the 2–3 nm range. It is often assumed that the dispersibility of the active phase is proportional to its length. The larger the dispersion degree, the shorter the active phase slabs are (Zhou et al., 2018). As a result, the degree of metal dispersion on the catalysts decreased in the following order: NiW/NiSAPO-11 > NiW/Ni-SAPO-11 > NiW/Ni@SAPO-11 > NiW/SAPO-11, which was consistent with the f_W values in **Table 3**. However, in addition to the length of WS_2 slabs, the number of WS_2 slabs stacked can have an impact on the properties of the active phase. The interaction between active metal and support is adequately reflected by the stacking number of WS_2 slabs (Zhou et al., 2017). The average stacking number of WS_2 slabs for NiW/SAPO-11 was only 1.33. There were about half of the monolayer WS_2 slabs, which were classified as the "type I active phase" with low de/hydrogenation activity. This can be explained by the fact that when tungsten species are loaded on SAPO-11, they form strong W-O-Al bonds with the support, and the interaction is too strong. The average stacking number of WS_2 slabs for NiW/Ni@SAPO-11 was 2.64, with around 33% of WS_2 slabs having stacking numbers ranging from 3 to 4. This could be due to a decrease in the L acid sites of Ni@SAPO-11, resulting in a weaker interaction between active phase and support. The average stacking number of WS_2 slabs in NiW/Ni-SAPO-11 was 3.23, with over 70% of WS_2 slabs having stacking numbers ranging from 3 to 4. Because of their moderate dispersibility and stacking number, NiW/NiSAPO-11 slabs had an average stacking number of 3.27, and around 85% of WS_2 slabs had 3-4 stacking layers, which are
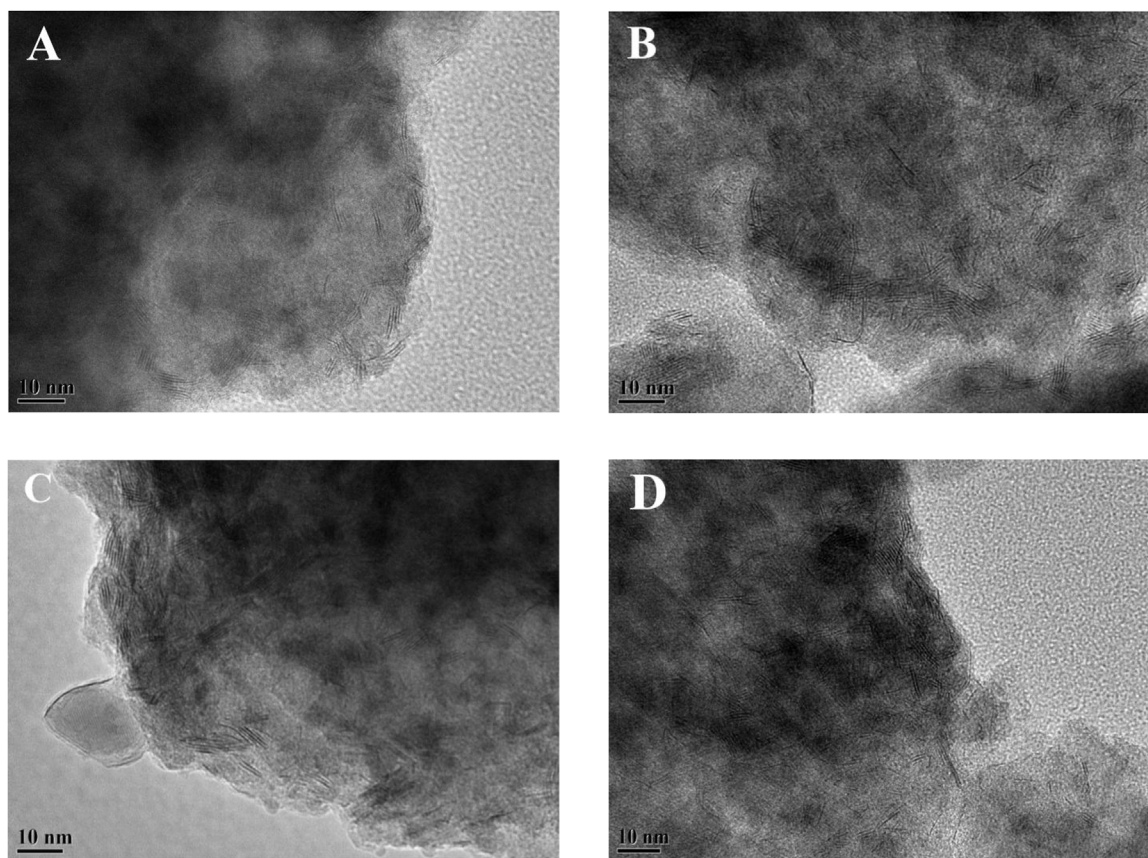
FIGURE 7 | Representative HRTEM images of sulfided catalysts: **(A)** NiW/SAPO-11, **(B)** NiW/Ni@SAPO-11, **(C)** NiW/Ni-SAPO-11, and **(D)** NiW/NiSAPO-11.

TABLE 3 | Average lengths, layer numbers, and f_W values of WS$_2$ of all catalysts.

Sample	$\bar{L}$ (nm)	$\bar{N}$	f_W
NiW/SAPO-11	4.62	1.33	0.28
NiW/Ni@SAPO-11	3.95	2.64	0.29
NiW/Ni-SAPO-11	2.98	3.23	0.31
NiW/NiSAPO-11	2.63	3.27	0.32

designated the "type II active phase" with good de/hydrogenation activity. This can be explained by the fact that when tungsten species are loaded on Ni-SAPO-11 and NiSAPO-11, they form W-O-Ni bonds with the support, and W-O-Ni bonds are weaker than W-O-Al bonds. Additional Ni species were coupled to the surface framework of SAPO-11 molecular sieves rather than the bulk phase during the complexation-excessive impregnation modification, resulting in the formation of more W-O-Ni species. EDTA can similarly "anchor" Ni species, allowing them to be evenly "anchored" in a specific place and hence uniformly integrated into the surface framework of the SAPO-11 molecular sieve. "Delumination and nickel supplementation" is the term for this phenomenon. Overall, among the Ni-modified SAPO-11-supported NiW catalysts, NiW/NiSAPO-11 had the best metal dispersibility and reducibility, as well as the highest hydrogenation activity.

The catalysts were studied using XPS to determine the covalent states of nickel and tungsten surface species on the sulfided catalysts. The W 4f XPS spectra and Ni 2p XPS spectra of the sulfided catalysts are shown in **Figures 8, 9**, respectively, and the binding energies (BE) and Sulfidation degree of tungsten and nickel species on the sulfided catalysts are provided in **Tables 4, 5**, respectively. The W 4f XPS spectra were decomposed into four peaks, each of which consisted of two overlapping W^{4+} and W^{6+} peaks. The W 4f$_{7/2}$ and W 4f$_{5/2}$ levels of W^{4+} (WS$_2$) have binding energies of around 32.70 ± 0.50 eV and 35.40 ± 0.50 eV, respectively, while the W 4f$_{7/2}$ and W 4f$_{5/2}$ levels of W^{6+} (WO$_3$) have binding energies of about 36.50 ± 0.50 eV and 38.30 ± 0.50 eV, respectively (Cui et al., 2012). The easy metals are to sulfide, the weaker the connection between the metal and the support, and the more metal layers there are. The percentage of W^{4+} species [W^{4+}/(W^{4+} + W^{6+})] has a significant impact on the catalytic performance of hydrotreating catalysts, hence the sulfidation degree of tungsten species on sulfided catalysts was estimated (Cui et al., 2013). The degree of sulfidation of tungsten species on different sulfided catalysts decreased in the order NiW/NiSAPO-11 (62.07%) > NiW/N-SAPO-11 (60.93%) > NiW/Ni@SAPO-11 (56.96%) > NiW/SAPO-11 (56.96%) > NiW/SAPO-11 (56.96%) > NiW/SAPO-11 (56.96%) > NiW/SAPO (54.29%). The decrease in interaction
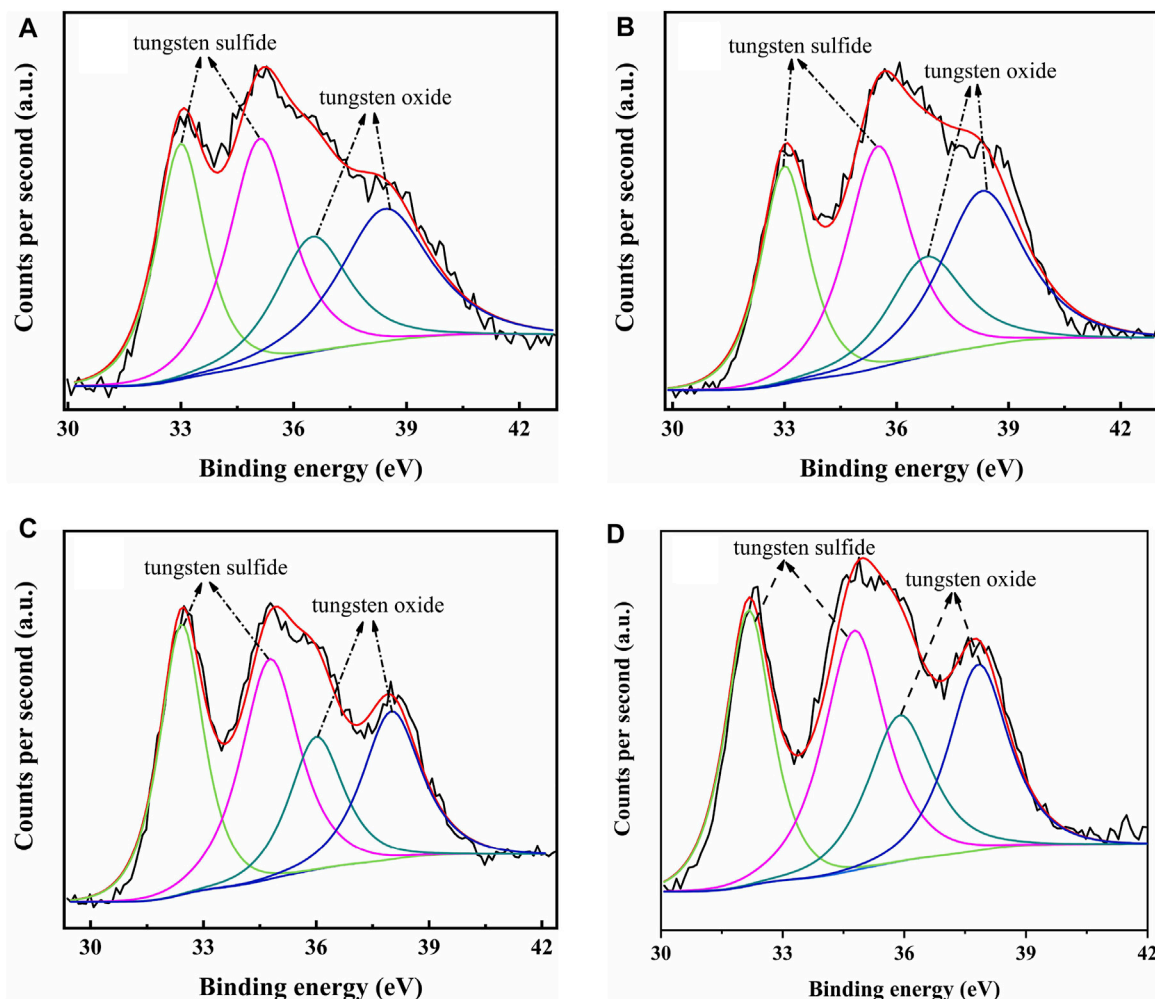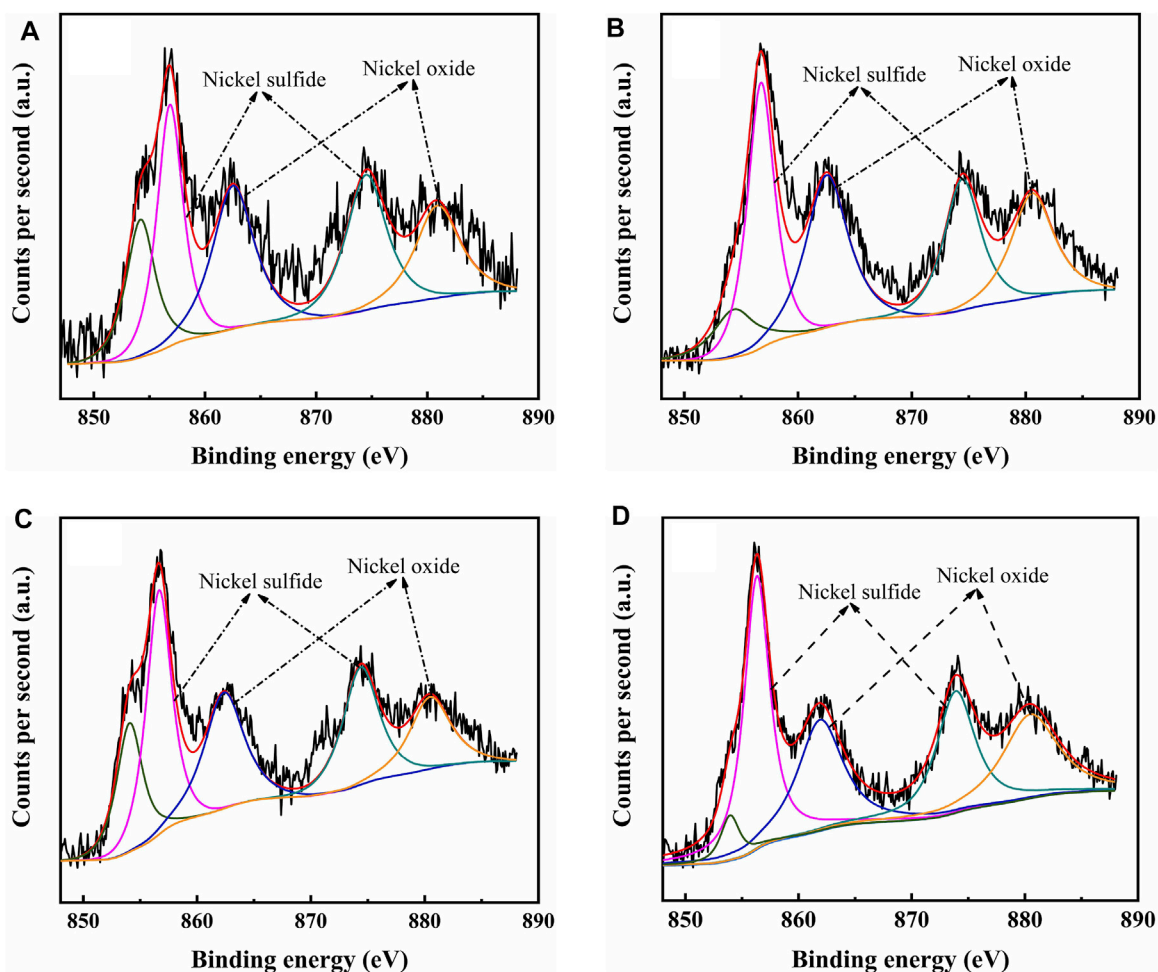
FIGURE 8 | XPS W 4f spectra of sulfided catalysts: **(A)** NiW/SAPO-11, **(B)** NiW/Ni@SAPO-11, **(C)** NiW/Ni-SAPO-11, and **(D)** NiW/NiSAPO-11.

between active metals and support causes the increase in sulfidation degree of tungsten species on NiW/NiSAPO-11, NiW/Ni-SAPO-11, and NiW/Ni@SAPO-11 as compared to NiW/SAPO-11. To some extent, BE value can reflect the interaction between metal species and support. **Table 4** shows that the BE values of tungsten species on the three catalysts, whether oxidic or sulfided, decrease in the order of NiW/SAPO-11 > NiW/Ni@SAPO-11 > NiW/Ni-SAPO-11 > NiW/NiSAPO-11. The results show that the interaction between tungsten species and support decreases in the order of NiW/SAPO-11 > NiW/Ni@SAPO-11 > NiW/Ni-SAPO-11 > NiW/NiSAPO-11, which is completely consistent with the results reflected by H_2-TPR and HRTEM. The Ni 2p XPS spectra were separated into five peaks, including two overlapping nickel oxide and nickel sulfide peaks. The Ni $2p_{3/2}$ and Ni $2p_{1/2}$ levels of nickel oxide (NiO) have binding energies of around 862.50 ± 0.50 eV and 880.50 ± 0.50 eV, respectively, while the Ni $2p_{3/2}$ and Ni $2p_{1/2}$ levels of nickel sulfide (NiS$_x$) have binding energies of about 856.50 ± 0.50 eV and 874.20 ± 0.50 eV, respectively (Yu et al., 2012). The sulfidation degree of nickel species was defined as the percentage

of nickel sulfide species [NiS$_x$/(NiO + NiS$_x$)] (Cui et al., 2013). The sulfidation degree of nickel species on different sulfided catalysts decreased in the order of NiW/NiSAPO-11 (52.23%) > NiW/Ni-SAPO-11 (49.13%) > NiW/Ni@SAPO-11 (48.35%) > NiW/SAPO-11 (45.41%), and the explanation for this change order is the same as that of tungsten species explained above.

Catalytic Performance

The catalyst was sulfurized ahead of time, and the reaction pressure was set to 2.0 MPa, LHSV was set at 1.5 h^{-1}, and H_2/oil was 600 (v/v) in a typical reaction. In the reaction temperature range of 300–400°C, the catalytic performance of the catalyst was studied. **Figure 10A** depicts n-C_{16} conversion on several catalysts at various reaction temperatures. The conversion on all catalysts increased with the increase in reaction temperature, as shown in **Figure 10A**. The catalytic activity of NiW/NiSAPO-11 was much higher than that of other catalysts. The catalytic activity of all the catalysts increased in the order of NiW/Ni@SAPO-11 < NiW/SAPO-11 < NiW/Ni-SAPO-11 < NiW/NiSAPO-11. The selectivity of all catalysts to i-hexadecane (i-C_{16}) reduced as

FIGURE 9 | XPS Ni 2p spectra of sulfided catalysts: **(A)** NiW/SAPO-11, **(B)** NiW/Ni@SAPO-11, **(C)** NiW/Ni-SAPO-11, and **(D)** NiW/NiSAPO-11.

TABLE 4 | Binding energy and sulfidation degree of W on different catalysts.

Sample	NiW/SAPO-11	NiW/Ni@SAPO-11	NiW/Ni-SAPO-11	NiW/NiSAPO-11
Oxidic	Binding energy (eV)			
W $4f_7$	36.70	36.50	36.10	35.82
W $4f_5$	38.43	38.30	38.00	37.78
Sulfided	Binding energy (eV)			
W $4f_7$	33.00	32.90	32.42	32.14
W $4f_5$	35.35	35.25	34.77	34.62
Sulfidation degree of W (%)	54.29	56.96	60.93	62.07

reaction temperature climbed, showing that the rate of cracking side reactions increased as reaction temperature increased **Figure 10C**. The selectivity of NiW/NiSAPO-11 to i-C$_{16}$ was clearly higher than that of NiW/SAPO-11, NiW/Ni@SAPO-11, and NiW/Ni-SAPO-11 within the reaction temperature range of catalytic performance evaluation (**Figure 10B**). This can be explained by the fact that NiSAPO-11 has the most medium and strong B acid sites, which are universally recognized as active sites for the isomerization of olefin intermediate skeletons (Yu et al., 2021). Furthermore, on NiW/Ni-SAPO-11, the interaction between active metals and support is weak, and the dispersibility and stacking number of the so-called NiWS active phase are moderate, resulting in good hydrogenation activity for isomeric olefin intermediates that diffuse from the acid to the metal sites. The interaction between the active metals and the support in NiW/SAPO-11 is strong, making it difficult to diminish the active metals and resulting in lower i-C$_{16}$ selectivity than NiW/Ni-SAPO-11. NiW/Ni@SAPO-11

TABLE 5 | Binding energy and sulfidation degree of Ni on different catalysts.

Sample	NiW/SAPO-11	NiW/Ni@SAPO-11	NiW/Ni-SAPO-11	NiW/NiSAPO-11
Oxidic	Binding energy (eV)			
Ni 2p$_3$	862.71	862.50	862.15	861.89
Ni 2p$_1$	880.90	880.57	880.26	880.11
Sulfided	Binding energy (eV)			
Ni 2p$_3$	856.84	856.74	856.65	856.35
Ni 2p$_1$	874.51	874.42	874.31	873.88
Sulfidation degree of Ni (%)	45.41	48.35	49.13	52.23
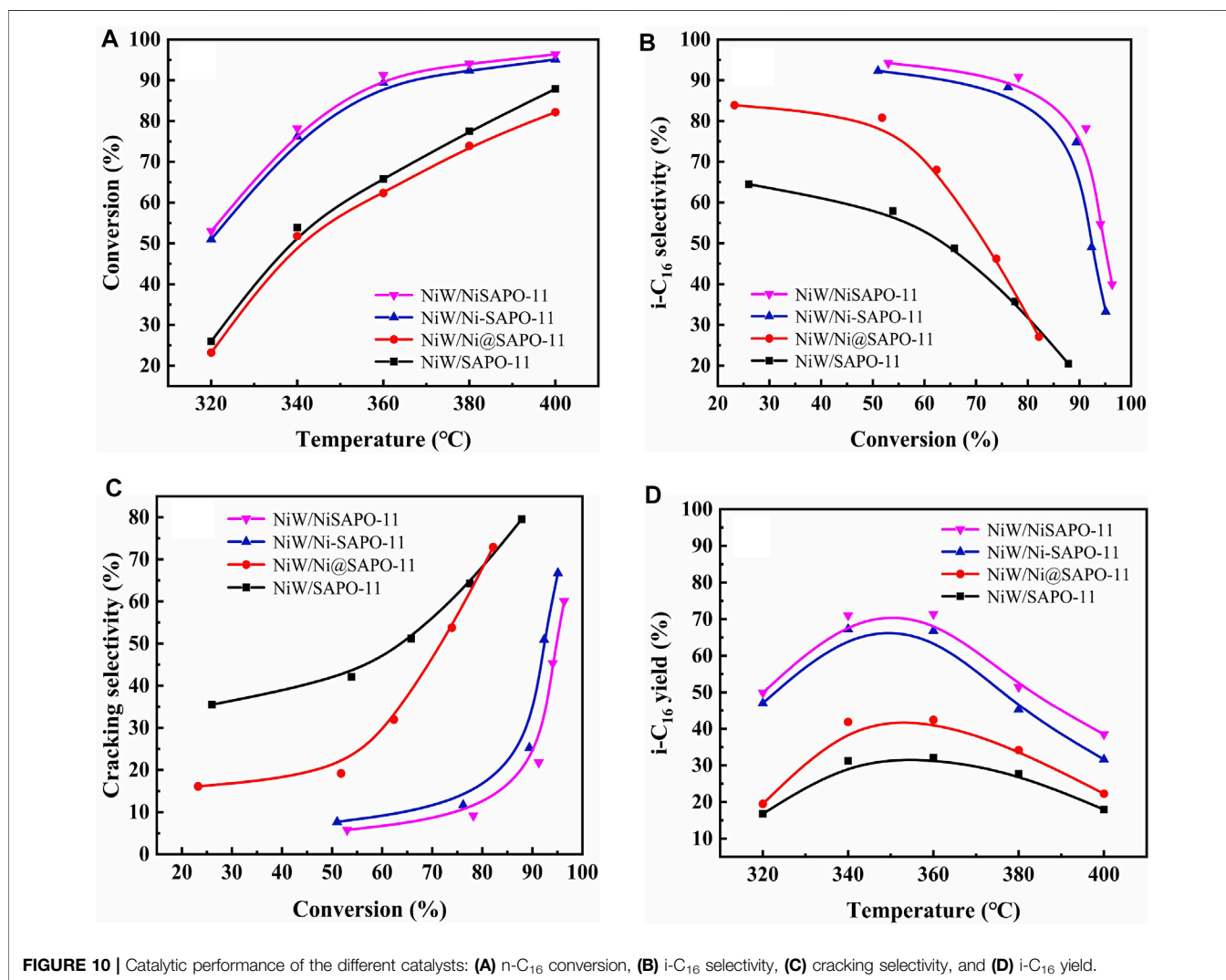
FIGURE 10 | Catalytic performance of the different catalysts: **(A)** n-C$_{16}$ conversion, **(B)** i-C$_{16}$ selectivity, **(C)** cracking selectivity, and **(D)** i-C$_{16}$ yield.

has the fewest medium and strong B acid sites, but its active phase dispersion degree and stacking number are higher than those of NiW/SAPO-11, resulting in lesser n-C$_{16}$ conversion and higher isomer selectivity than NiW/SAPO-11. **Figure 10D** shows the yield of i-C$_{16}$ for various catalysts, and the yield of i-C$_{16}$ for NiW/NiSAPO-11 is clearly higher than the other three catalysts. The maximum yield of i-C$_{16}$ of different catalysts increased in the order of NiW/SAPO-11

(32.10%) > NiW/Ni@SAPO-11 (42.41%) > NiW/Ni-SAPO-11 (66.82%) > NiW/NiSAPO-11 (71.40%). These results indicate that the complexation-excessive impregnation-modified SAPO-11-supported NiWS catalyst has a better catalytic performance than that of ion-exchange modified SAPO-11 support NiWS catalyst, unmodified SAPO-11-supported NiWS catalyst, and *in situ* Ni-modified SAPO-11 support NiWS catalyst for n-hexadecane hydroisomerization.

TABLE 6 | Isomer distributions, TOF values, and k_{iso} values of n-C_{16} hydroisomerization over the different catalysts at 340 °C.

Products	Selectivity (%)			
	NiW/SAPO-11	NiW/Ni@SAPO-11	NiW/Ni-SAPO-11	NiW/NiSAPO-11
Selectivity of C_{16} (%)	57.92	80.81	88.30	90.81
TOF (h^{-1})	26.29	26.72	30.41	31.22
k_{iso} (mol g^{-1} h^{-1})	7.26×10^{-3}	5.80×10^{-3}	1.16×10^{-2}	1.21×10^{-2}
2-MC_{15}	13.57	16.99	17.87	19.77
3-MC_{15}	13.65	19.07	20.43	18.25
4-MC_{15}	7.17	12.74	13.27	16.31
5-MC_{15}	7.18	8.81	10.01	8.78
6-MC_{15}	4.54	5.41	5.95	6.17
2,4-DMC_{14}	3.10	4.18	5.72	5.69
2,5-DMC_{14}	2.92	4.23	4.91	4.42
2,6-DMC_{14}	1.98	3.31	3.35	3.87
3,6-DMC_{14}	1.13	1.88	2.37	3.03
3,7-DMC_{14}	0.77	1.21	1.38	1.77
3-EC_{14}	0.43	0.73	0.76	1.13
5-EC_{14}	0.38	0.78	0.83	0.97
6-EC_{14}	0.32	0.55	0.48	0.55
5,8-DEC_{12}	0.28	0.44	0.25	0.45
Others	0.50	0.48	0.72	0.65

The isomer product distributions, TOF values and k_{iso} values of different catalysts at 340°C are presented in **Table 6**. The reaction rate constants of different catalysts increased in the order of NiW/Ni@SAPO-11 (5.80×10^{-3} mol g^{-1} h^{-1}) < NiW/SAPO-11 (7.26×10^{-3} mol g^{-1} h^{-1}) < NiW/Ni-SAPO-11 (1.16×10^{-2} mol g^{-1} h^{-1}) < NiW/NiSAPO-11 (1.21×10^{-2} mol g^{-1} h^{-1}), which is due to the difference between the amount of medium and strong B acid in the three supports. While the TOF values of the three catalysts decreased in the order of NiW/NiSAPO-11 ($31.22 \, h^{-1}$) > NiW/Ni-SAPO-11 ($30.41 \, h^{-1}$) > NiW/Ni@SAPO-11 ($26.72 \, h^{-1}$) > NiW/SAPO-11 ($26.29 \, h^{-1}$), and the calculated TOF values well verified the catalytic activity of the catalysts. This result can be explained by the fact that the weakening of the interaction between the active phase and the support promoted more active phases to form "type II active phase", which increased the desorption rate of carbocation on the active phase. The isomer products of different catalysts were mainly mono-branched isomer products, and monomethyl branched isomer products were the main mono-branched isomer products.

CONCLUSION

The ion-exchange method, *in situ* synthesis method, and complexation-excessive impregnation modification method successfully prepared Ni-modified SAPO-11 molecular sieves, and the corresponding NiW-supported catalysts were successfully prepared by the incipient-wetness impregnation method, and then used for hydroisomerization of n-hexadecane. The effects of several Ni-modification procedures on the properties of SAPO-11, particularly the active phase properties on the related catalysts, were studied. The results showed that the crystal structure of Ni@SAPO-11 prepared by the ion-exchange method collapsed partially, and nickel species occupied a portion of the pore volume and covered a portion of the acid sites, resulting in a drop in specific surface area, pore volume, and acid sites amount. Ni-SAPO-11 produced *in situ* had a larger specific surface area, pore volume, and medium and strong Brønsted acid sites. However, during dealumination, EDTA had the effect of dredging channels and reaming holes, resulting in a larger BET specific surface area and pore volume of NiSAPO-11. Furthermore, EDTA made it simple to incorporate Ni species into the surface framework of the SAPO-11 molecular sieve rather than the bulk phase, resulting in NiSAPO-11 with better acidity. The support of NiW/NiSAPO-11 had the most Brønsted acid sites, the weakest interaction between active metals and support, and the highest dispersibility and stacking number of active phase, all of which were helpful to n-hexadecane hydroisomerization. NiW/NiSAPO-11 had much greater n-C_{16} conversion, i-C_{16} selectivity, and i-C_{16} yield than the other catalysts. It is expected to provide theoretical guidance for the design of high-activity non-noble metal catalysts for the hydroisomerization of alkanes.

DATA AVAILABILITY STATEMENT

The original contributions presented in the study are included in the article/Supplementary Material, further inquiries can be directed to the corresponding author.

AUTHOR CONTRIBUTIONS

XD designed experimental plans, performed main experimental work, analyzed and discussed results, and wrote the manuscript. YC assisted in the design of the scheme, performed the main experimental work and assisted in literature review and manuscript sorting. MS

participated in the manuscript writing. QW proposed the themes, ideas, and content of the manuscript research work, assisted in literature review and manuscript sorting. YZ guided experimental work and manuscript revision.

REFERENCES

Blasco, T., Chica, A., Corma, A., Murphy, W., Agundezrodriguez, J., and Perezpariente, J. (2006). Changing the Si Distribution in SAPO-11 by Synthesis with Surfactants Improves the Hydroisomerization/dewaxing Properties. *J. Catal.* 242 (1), 153–161. doi:10.1016/j.jcat.2006.05.027

Chen, Z., Dong, Y., Jiang, S., Song, W., Lai, W., Yi, X., et al. (2017). Low-temperature Synthesis of Hierarchical Architectures of SAPO-11 Zeolite as a Good Hydroisomerization Support. *J. Mater. Sci.* 52 (8), 4460–4471. doi:10.1007/s10853-016-0692-z

Cui, Q., Wang, S., Wei, Q., Mu, L., Yu, G., Zhang, T., et al. (2019). Synthesis and Characterization of Zr Incorporated Small crystal Size Y Zeolite Supported NiW Catalysts for Hydrocracking of Vacuum Gas Oil. *Fuel* 237, 597–605. doi:10.1016/j.fuel.2018.10.040

Cui, Q., Zhou, Y., Wei, Q., Tao, X., Yu, G., Wang, Y., et al. (2012). Role of the Zeolite Crystallite Size on Hydrocracking of Vacuum Gas Oil over NiW/Y-ASA Catalysts. *Energy Fuels* 26 (8), 4664–4670. doi:10.1021/ef300544c

Cui, Q., Zhou, Y., Wei, Q., Yu, G., and Zhu, L. (2013). Performance of Zr- and P-Modified USY-Based Catalyst in Hydrocracking of Vacuum Gas Oil. *Fuel Process. Tech.* 106, 439–446. doi:10.1016/j.fuproc.2012.09.010

Díaz de León, J. N., Zavala-Sánchez, L. A., Suárez-Toriello, V. A., Alonso-Núñez, G., Zepeda, T. A., Yocupicio, R. I., et al. (2017). Support Effects of NiW Catalysts for Highly Selective Sulfur Removal from Light Hydrocarbons. *Appl. Catal. B: Environ.* 213, 167–176.

Du, Y., Feng, B., Jiang, Y., Yuan, L., Huang, K., and Li, J. (20182018). Solvent-Free Synthesis and N -Hexadecane Hydroisomerization Performance of SAPO-11 Catalyst. *Eur. J. Inorg. Chem.* 2018 (22), 2599–2606. doi:10.1002/ejic.201800134

Du, Y., Yao, H., Zhao, L., Yang, H., Wang, M., Yuan, L., et al. (2019). Graphene Oxide Induced High Crystallinity of SAPO-11 Molecular Sieves for Improved Alkane Isomerization Performance. *ChemNanoMat* 5 (9), 1225–1232. doi:10.1002/cnma.201900349

Guo, L., Bao, X., Fan, Y., Shi, G., Liu, H., and Bai, D. (2012). Impact of Cationic Surfactant Chain Length during SAPO-11 Molecular Sieve Synthesis on Structure, Acidity, and N-Octane Isomerization to Di-methyl Hexanes. *J. Catal.* 294, 161–170. doi:10.1016/j.jcat.2012.07.016

Guo, L., Fan, Y., Bao, X., Shi, G., and Liu, H. (2013). Two-stage Surfactant-Assisted Crystallization for Enhancing SAPO-11 Acidity to Improve N-Octane Di-branched Isomerization. *J. Catal.* 301, 162–173. doi:10.1016/j.jcat.2013.02.001

Hongloi, N., Prapainainar, P., and Prapainainar, C. (2021). Review of green Diesel Production from Fatty Acid Deoxygenation over Ni-Based Catalysts. *Mol. Catal.*, 111696. doi:10.1016/j.mcat.2021.111696

Jin, D., Li, L., Ye, G., Ding, H., Zhao, X., Zhu, K., et al. (2018). Manipulating the Mesostructure of Silicoaluminophosphate SAPO-11 via Tumbling-Assisted, Oriented Assembly Crystallization: a Pathway to Enhance Selectivity in Hydroisomerization. *Catal. Sci. Technol.* 8 (19), 5044–5061. doi:10.1039/c8cy01483c

Karthikeyan, D., Atchudan, R., and Sivakumar, R. (2016). Effect of Metal Content on the Activity and Product Selectivity of N-Decane Hydroisomerization over Ni-Pd/HY Zeolite. *Chin. J. Catal.* 37, 1907–1917. doi:10.1016/s1872-2067(16)62507-x

Li, X., and Wu, D. (2020). Synthesis of Co-doped Micro-mesoporous SAPO-11 Zeolite for Glycerol Hydrogenolysis. *Korean J. Chem. Eng.* 37 (2), 216–223. doi:10.1007/s11814-019-0445-1

Liu, Q., Zuo, H., Wang, T., Ma, L., and Zhang, Q. (2013). One-step Hydrodeoxygenation of palm Oil to Isomerized Hydrocarbon Fuels over Ni Supported on Nano-Sized SAPO-11 Catalysts. *Appl. Catal. A: Gen.* 468, 68–74. doi:10.1016/j.apcata.2013.08.009

Lyu, Y., Liu, Y., Xu, L., Zhao, X., Liu, Z., Liu, X., et al. (2017). Effect of Ethanol on the Surface Properties and N-Heptane Isomerization Performance of Ni/SAPO-11. *Appl. Surf. Sci.* 401, 57–64. doi:10.1016/j.apsusc.2016.12.230

Lyu, Y., Yu, Z., Yang, Y., Liu, Y., Zhao, X., Liu, X., et al. (2019). Metal and Acid Sites Instantaneously Prepared over Ni/SAPO-11 Bifunctional Catalyst. *J. Catal.* 374, 208–216. doi:10.1016/j.jcat.2019.04.031

Lyu, Y., Yu, Z., Yang, Y., Wang, X., Zhao, X., Liu, X., et al. (2019). Metal-acid Balance in the In-Situ Solid Synthesized Ni/SAPO-11 Catalyst for N-Hexane Hydroisomerization. *Fuel* 243, 398–405. doi:10.1016/j.fuel.2019.01.013

Lyu, Y., Zhan, W., Wang, X., Yu, Z., Liu, X., and Yan, Z. (2020). Regulation of Synergy between Metal and Acid Sites over the Ni-SAPO-11 Catalyst for N-Hexane Hydroisomerization. *Fuel*, 274, 117855.

Minaev, P. P., Nikul'shina, M. S., Mozhaev, A. V., and Nikul'shin, P. A. (2019). NiWS/Al2O3 Diesel Fraction Deep Hydrotreating Catalyst Synthesized Using Mesostructured Aluminum Hydroxide. *Pet. Chem.* 58 (14), 1186–1191. doi:10.1134/s0965544118140098

Pimerzin, A. A., Roganov, A. A., Verevkin, S. P., Konnova, M. E., Pilshchikov, V. A., and Pimerzin, A. A. (2019). Bifunctional Catalysts with noble Metals on Composite Al2O3-SAPO-11 Carrier and Their Comparison with CoMoS One in N-Hexadecane Hydroisomerization. *Catal. Today* 329, 71–81. doi:10.1016/j.cattod.2018.12.034

Shi, G., Fang, D., and Shen, J. (2009). Hydroisomerization of Model FCC Naphtha over Sulfided Co(Ni)-Mo(W)/MCM-41 Catalysts. *Microporous Mesoporous Mater.* 120 (3), 339–345. doi:10.1016/j.micromeso.2008.11.022

Song, X., Bai, X., Wu, W., Kikhtyanin, O. V., Zhao, A., Xiao, L., et al. (2017). The Effect of Palladium Loading on the Catalytic Performance of Pd/SAPO-11 for N-Decane Hydroisomerization. *Mol. Catal.* 433, 84–90. doi:10.1016/j.mcat.2016.12.017

Tan, Y., Hu, W., Du, Y., and Li, J. (2021). Species and Impacts of Metal Sites over Bifunctional Catalyst on Long Chain N-Alkane Hydroisomerization: A Review. *Appl. Catal. A: Gen.* 611. doi:10.1016/j.apcata.2020.117916

Tao, S., Li, X., Lv, G., Wang, C., Xu, R., Ma, H., et al. (2017). Highly Mesoporous SAPO-11 Molecular Sieves with Tunable Acidity: Facile Synthesis, Formation Mechanism and Catalytic Performance in Hydroisomerization of N-Dodecane. *Catal. Sci. Technol.* 7 (23), 5775–5784. doi:10.1039/c7cy01819c

Tao, X., Zhou, Y., Wei, Q., Yu, G., Cui, Q., Liu, J., et al. (2014). Effect of Morphology Properties of NiW Catalysts on Hydrodesulfurization for Individual Sulfur Compounds in Fluid Catalytic Cracking Diesel. *Fuel Process. Tech.* 118, 200–207. doi:10.1016/j.fuproc.2013.08.023

Tian, S., and Chen, J. (2014). Hydroisomerization of N-Dodecane on a New Kind of Bifunctional Catalyst: Nickel Phosphide Supported on SAPO-11 Molecular Sieve. *Fuel Process. Tech.* 122, 120–128. doi:10.1016/j.fuproc.2014.01.031

Tiuliukova, I. A., Rudina, N. A., Lysikov, A. I., Cherepanova, S. V., and Parkhomchuk, E. V. (2018). Screw-like Morphology of Silicoaluminophosphate-11 (SAPO-11) Crystallized in Ethanol Medium. *Mater. Lett.* 228, 61–64. doi:10.1016/j.matlet.2018.05.118

Wang, J., Zhang, W., Suo, Y., and Wang, Y. (2018). Synthesis of Ni/H-Zr-MCM-48 and Their Isomerization Activity of N-Heptane. *J. Porous Mater.* 25, 1317–1324. doi:10.1007/s10934-017-0542-7

Wei, X., Kikhtyanin, O. V., Parmon, V. N., Wu, W., Bai, X., Zhang, J., et al. (2017). Synergetic Effect between the Metal and Acid Sites of Pd/SAPO-41 Bifunctional Catalysts in N-Hexadecane Hydroisomerization. *J. Porous Mater.* 25 (1), 235–247. doi:10.1007/s10934-017-0437-7

Wen, C., Wang, X., Xu, J., and Fan, Y. (2019). *Hierarchical SAPO-11 Mol. sieve-based catalysts enhancing double-branched hydroisomerization alkanesFuel* 255. doi:10.1016/j.fuel.2019.115821

Wen, C., Xu, J., Wang, X., and Fan, Y. (2020). n-Heptane Hydroisomerization over a SO42-/ZrO2@SAPO-11 Composite-Based Catalyst Derived from the Growth of UiO-66 on SAPO-11. *Energy Fuels* 34 (8), 9498–9508. doi:10.1021/acs.energyfuels.0c01634

Yang, L., Xing, S., Sun, H., Miao, C., Li, M., Lv, P., et al. (2019). Citric-acid-induced Mesoporous SAPO-11 Loaded with Highly Dispersed Nickel for Enhanced Hydroisomerization of Oleic Acid to Iso-Alkanes. *Fuel Process. Tech.* 187, 52–62. doi:10.1016/j.fuproc.2019.01.008

Yang, Z., Li, J., Liu, Y., and Liu, C. (2017). Effect of Silicon Precursor on Silicon Incorporation in SAPO-11 and Their Catalytic Performance for Hydroisomerization of N -octane on Pt-Based Catalysts. *J. Energ. Chem.* 26 (4), 688–694. doi:10.1016/j.jechem.2017.02.002

Yang, Z., Liu, Y., Li, Y., Zeng, L., Liu, Z., Liu, X., et al. (2019). Effect of Preparation Method on the Bimetallic NiCu/SAPO-11 Catalysts for the Hydroisomerization of N-Octane. *J. Energ. Chem.* 28, 23–30. doi:10.1016/j.jechem.2017.10.003

Yang, Z., Liu, Y., Liu, D., Meng, X., and Liu, C. (2017). Hydroisomerization of N -octane over Bimetallic Ni-Cu/SAPO-11 Catalysts. *Appl. Catal. A: Gen.* 543, 274–282. doi:10.1016/j.apcata.2017.06.028

Yang, Z., Liu, Y., Zhao, J., Gou, J., Sun, K., and Liu, C. (2017). Zinc-modified Pt/ SAPO-11 for Improving the Isomerization Selectivity to Dibranched Alkanes. *Chin. J. Catal.* 38 (3), 509–517. doi:10.1016/s1872-2067(17)62755-4

Yu, G., Qiu, M., Wang, T., Ge, L., Chen, X., and Wei, W. (2021). Optimization of the Pore Structure and Acidity of SAPO-11 for Highly Efficient Hydroisomerization on the Long-Chain Alkane. *Microporous Mesoporous Mater.* 320. doi:10.1016/j.micromeso.2021.111076

Yu, G., Zhou, Y., Wei, Q., Tao, X., and Cui, Q. (2012). A Novel Method for Preparing Well Dispersed and Highly Sulfided NiW Hydrodenitrogenation Catalyst. *Catal. Commun.* 23, 48–53. doi:10.1016/j.catcom.2012.03.002

Zhang, P., Liu, H., Yue, Y., Zhu, H., and Bao, X. (2018). Direct Synthesis of Hierarchical SAPO-11 Molecular Sieve with Enhanced Hydroisomerization Performance. *Fuel Process. Tech.* 179, 72–85. doi:10.1016/j.fuproc.2018.06.012

Zhao, L., Hu, Y., Wang, Y., and Ma, S. (2014). Preparation and Property of Ni/ TiO2-SAPO-11 Catalyst for N-Heptane Isomerization. *Mrc* 03, 63–67. doi:10. 4236/mrc.2014.33009

Zhou, W., Zhang, Y., Tao, X., Zhou, Y., Wei, Q., and Ding, S. (2018). Effects of Gallium Addition to Mesoporous Alumina by Impregnation on Dibenzothiophene Hydrodesulfurization Performances of the Corresponding NiMo Supported Catalysts. *Fuel* 228, 152–163. doi:10.1016/j.fuel.2018.04.084

Zhou, W., Zhou, Y., Wei, Q., Zhang, Y., Zhang, Q., Jiang, S., et al. (2017). Gallium Modified HUSY Zeolite as an Effective Co-support for NiMo Hydrodesulfurization Catalyst and the Catalyst's High Isomerization Selectivity. *Chem. Eur. J.* 23 (39), 9369–9382. doi:10.1002/chem.201701307